Temporal Properties of Accretion around Black Holes

by

Tejas Sewak

1020201511

Ashoka University, Sonepat

A thesis submitted to the

Physics Department

in partial fulfillment of requirements

for the Degree of

Postgraduate Diploma in Advanced Studies and Research

of

Ashoka University

May, 2021

STATEMENT BY AUTHOR

This dissertation has been submitted in partial fulfillment of requirements for an degree at Ashoka University and is deposited in the Library to be made available to borrowers under rules of Ashoka University.

Brief quotations from this dissertation are allowable without special permission, provided that accurate acknowledgement of source is made. Requests for permission for extended quotation from, or reproduction of this manuscript in whole or in part, may be granted by the Competent Authority of Ashoka University when in his or her judgement the proposed use of the material is in the interests of scholarship. In all other instances, however, permission must be obtained from the author.

Tejas Sewak

DECLARATION

I hereby declare that the investigation presented in the thesis has been carried out by me. The work is original and has not been submitted earlier as a whole or in part for a degree/diploma at this or any other Institution/University.

Tejas Sewak

Acknowledgements

I want to take this opportunity to express my sincere gratitude to Professor Dipankar Bhattacharya, my thesis advisor, for offering me this project. His guidance, constant support, and timely encouragement always motivated me to perform to the best of my capabilities. His expertise in the field and dedication to teaching have undeniably inspired me to strive for excellence as a physicist. I am also incredibly grateful to Prof. Kandaswamy Subramanian, Prof. Jean Surdej and Dr. Kuntal Misra for allowing me to work on projects with them. This past year has made me realise that an academic life is worth pursuing.

I am also thankful to all my friends at Ashoka for their unwavering support during this project. Thank you all for checking up on my sleep after countless late-night study sessions. I am most grateful to Anjali for all the support and care she has provided me during this time.

I am incredibly grateful to my parents, whose constant love, comfort, and care have allowed me to achieve better things in life. Thank you for always giving me the freedom and support to pursue my dreams. I dedicate this project to you both.

Contents

Chapter 1

Introduction

This thesis aims to discuss the fast variability properties of Low Mass X-ray binary sources. The fast variability can help discern crucial information regarding the accretion geometry of the source. This chapter briefly explains what black hole X-ray binaries are and how we can observe these sources. We will also explain why we should study these sources.

1.1 X-ray binaries

Accretion onto black holes is one of the most efficient energy sources in the universe. It can lead to various luminous sources, including quasars, AGNs, black hole X-ray transients and violent phenomena such as tidal disruption events and X-ray bursts. While the size and mass of the source and energy released during such processes can vary by orders of magnitude, the physics of accretion is believed to scale accordingly in these systems. The astrophysical source of interest to us is an X-ray binary. This thesis studies the accretion properties through a detailed analysis of one such galactic black hole X-ray binary source called GRS 1915+105.

Binary systems, where two stars orbit around a common centre of mass, are common

in our universe. Suppose one of the objects in a binary system is a compact object, i.e., either a black hole or a neutron star, and the thermal energy generated during accretion is radiated in X-rays. In that case, such a source is called an X-ray binary. The compact object is called an accretor, and the normal star is called a donor or a companion star.

Depending on the mass of the donor star, X-ray binaries are classified into two categories: high-mass X-ray binaries (HMXB) and low-mass X-ray binaries (LMXB). If the mass of the donor star is higher than the mass of the compact object, then the X-ray binary is classified as an HMXB. Usually, the donor star mass is above $10 M_\odot$ and is a young, luminous star of type O or B. The donor star radiates in the optical band and is very luminous; thus, detecting the HMXB source is easier.
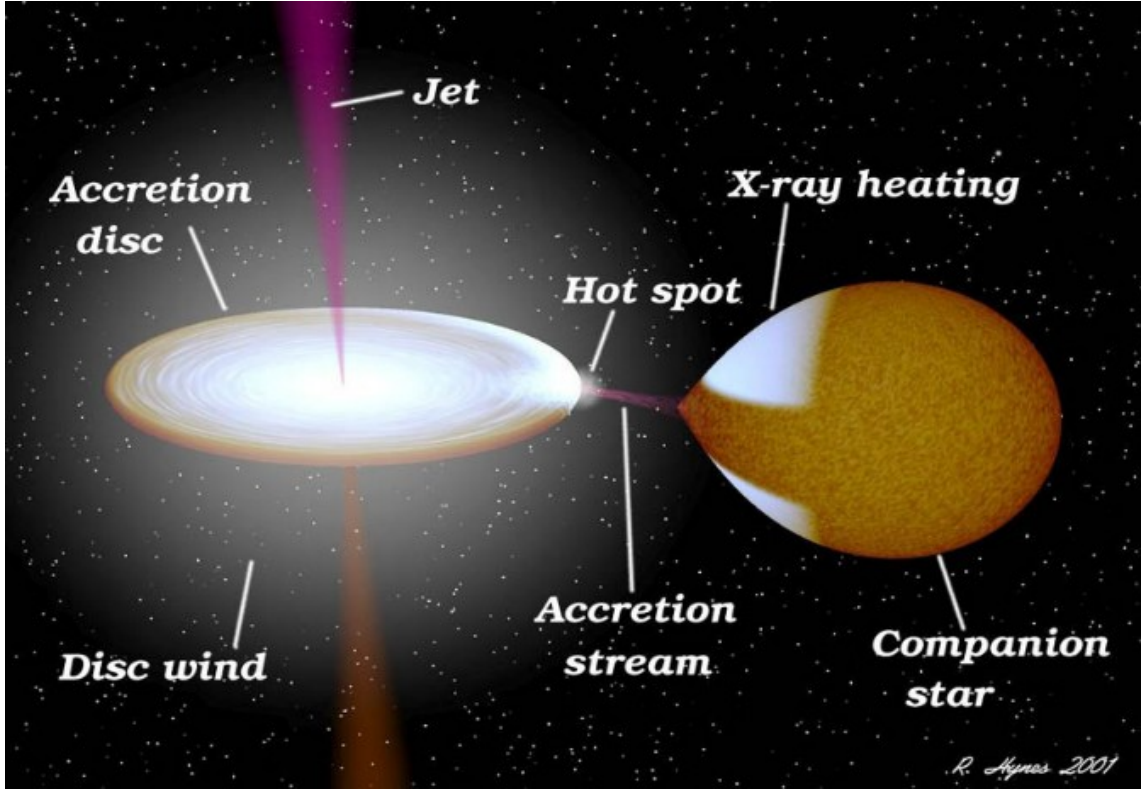

Figure 1.1: Artist's impression of an X-ray binary system. Important components of an accretion system are all marked. Credit: R Hynes)

However, if the mass of the donor star is less than the mass of the compact object, then the X-ray binary is classified as a LMXB. Here, the donor star mass is $\lesssim 1 M_\odot$.

These systems are among the older population of stars. The donor star is less luminous and does not radiate in the optical band. These sources are thus detected in X-rays when they are actively accreting. To date, there are ∼ 200 confirmed and candidate LMXBs identified in our Galaxy through their X-ray properties (Bambi and Sangangelo, 2022). Although identifying a compact object in the source is possible, the exact nature, i.e., whether a black hole or a neutron star exists, remains to be identified for several X-ray binary candidates (Bambi and Sangangelo, 2022). Accreting black hole systems, which are of focus in this thesis, are more commonly found in LMXBs than in HMXBs. This could either result from binary evolution (Bambi and Sangangelo, 2022) or observational biases.
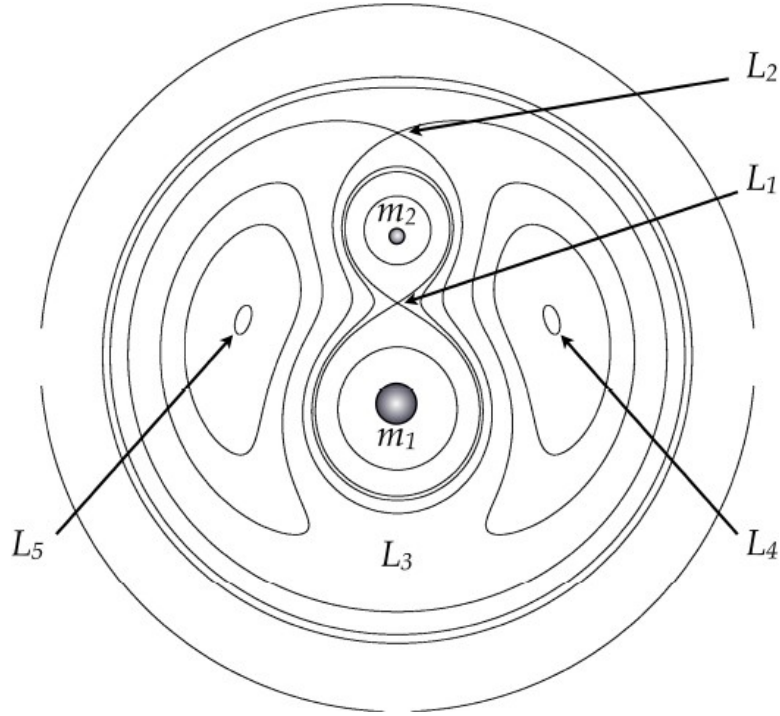
Figure 1.2: Accretion in LMXBs occurs due to Roche Lobe overflow through the L1 point.

Since the mass of the donor star and evolution stage is typically different for LMXBs and HMXBs, the accretion proceeds through different methods. For LMXBs, the matter transfer proceeds because of Roche Lobe overflow. The Roche Potential is the equipotential surface in the co-rotating frame of the binary system. The lobes through the L1 point that encircles the two stars are called the "Roche lobes". If

the donor star evolves and fills its Roche Lobe to reach the L1 point, the matter would gravitationally flow to the companion star (compact object). However, for most HMXBs, the massive star is not near its Roche Lobe limit, and stellar winds are responsible for carrying matter from the donor to the accretor in HMXBs. Since our focus is on LMXBs, the discussion on HMXBs here is limited.

Accreting matter cannot fall straight to the compact object as it has angular momentum. When this angular momentum $j \gg R_g c$, where R_g is the Schwarzchild radius of the black hole, an accretion disk is formed around the accretor and the matter orbits circularly at a certain radius from the accreting object. The viscous dissipation then helps the matter to distribute into an accretion disk. The accretion disk is maintained because of the turbulence generated due to the magneto-rotational instability in the accreting material. Even a weak magnetic field can make the flow turbulent. This instability allows the angular momentum to transfer towards the outside and matter to fall inside. There is a last circular orbit at a radius $R \sim j^2/R_g c^2$ and in principle, MRI effects can allow the matter to go as close to this Innermost Stable Circular Orbit (ISCO) (Karpouzas, 2021). During this process, the viscous heating converts gravitational binding energy to thermal energy and is radiated away from the disk. However, in the innermost regions of accretion, i.e., very close to the compact object, the most amount of gravitational potential energy is lost, and the radiation emitted is in X-ray.

1.2 Motivation to study X-ray Binaries

1. **Shorter dynamical time scales than AGNs:** Despite extensive research on accretion disks and relativistic jets in all kinds of compact objects, the exact nature of their physical connection remains an open question. The stellar mass black holes offer a unique opportunity to study the disk-jet connection and geometry of accreting

sources. These sources show changes in accretion dynamics at human-accessible time scales. Additionally, their high flux and abundance in our galaxy make them easier to study. Once we obtain the results regarding accretion physics for these smaller objects, we can generalise it to supermassive black holes in AGNs after appropriate scaling.

2.**Strong gravitational fields:** X-ray binaries are strong gravitational potential and high curvature objects. Such strong gravitational fields make them valuable small-scale laboratories for testing the theory of general relativity. For example, the origin of Quasi-Periodic Oscillations observed in the X-ray binaries has been widely interpreted in terms of relativistic frequencies, such as the Lense-Thirring Precession frequencies. Studying these QPOs in X-ray binaries offers an opportunity to verify properties observed in a strong-field gravity regime.

1.3   Project Outline

This thesis aims to interpret the accretion geometry and dynamics of the system by studying the temporal properties of accretion in low-mass X-ray binaries. The rest of the chapters are organised in the following manner. Chapter 2 describes the instruments used to observe the temporal and spectral variability in LMXRBs and techniques applied to analyse the data. Chapter 3 describes the past work done on BH LMXRBs, particularly on GRS 1915+105. Chapter 4 discusses the AstroSat observations used for this thesis and the procedure for obtaining the results. Chapter 5 presents the results of this thesis, while Chapter 6 discusses the interpretation of the obtained results in light of a variable Comptonization model.

Chapter 2

Instrumentation and Techniques

*In this chapter, we will describe the instruments used to observe X-ray binaries'
spectral and temporal properties. We will then explain the Fourier methods used
to study the temporal variability for such sources.*

2.1   Instruments

The analysis presented in this report is based on the data available from the Large
Area X-ray Proportional Counter instrument onboard the Indian satellite AstroSat,
which was launched in 2015. There are three proportional counters to collect the
event data, and complete information from individual photons for timing (light
curve) and spectral studies (time-averaged energy spectrum) is available. A propor-
tional counter is a sealed container with a window where X-rays enter when pointed
precisely towards the source. The container is filled with a mixture of gas. An X-ray
entering the container will interact with the gas, causing a cascade of electrons at
the electrodes. The main principle of a proportional counter is that the energy of
the incoming photons is proportional to the large number of electrons created in the
chamber and detected at the anodes. The large detection volume (15 cm depth)

filled with a mixture of xenon gas (90%) and methane (10%) results in detection efficiency greater than 50%, above 30 keV for the LAXPC instrument (Agrawal et al., 2017),. The LAXPC operates in the energy range of $3-80$ keV and with a temporal resolution of 10μs. Thus, it is best suited for both X-ray timing and spectral studies.
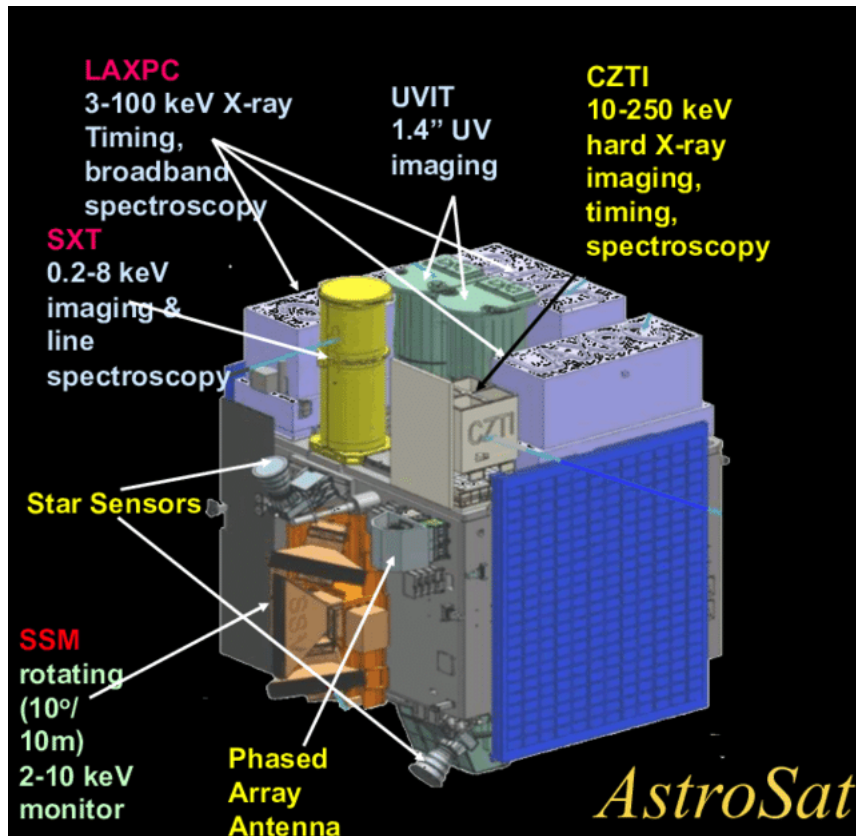
Figure 2.1: Schematic of the AstroSat. The three LAXPC instruments which provide a spectral range in 3-80 keV are marked in the figure. Data for this thesis is from these three LAXPC units.

2.2 Techniques

Observations of X-ray binaries are known to show variability in their emission. Since the X-rays are emitted in regions very close to the compact object, studying variability allows one to examine how the matter falling onto the compact object changes with time. We use two main timing techniques to study this variability: Power Density Spectrum and Cross Spectrum, which are discussed in the following subsections.

2.2.1 Power Density Spectrum

First, we have a time series of the X-ray emission called a light curve. The primary method to study the variability in this light curve is a Fourier Power Spectrum (PS or Power Density Spectrum PDS) of the light curve. A PDS is defined as the modulus squared of the Fourier transform of a light curve.

$$P(\nu) = F(\nu) \cdot F^*(\nu) = |F(\nu)|^2$$

This gives the measure of variability in terms of a Power density (P_ν) at a particular frequency ν. If oscillations at any specific frequency (or short range of frequencies) are preferred in the system, they will translate into sharp peaks (or quasi peaks) in the Power Density Spectrum. Therefore, a Power Density Spectrum provides a method to measure the periodic or quasi-periodic variability in the light curve. For LMXBs, the PDS show Quasi-Periodic Oscillations (QPOs) across a range of frequencies. Even for the same source, the QPO peaks vary in amplitude and frequency for different observations. The quasi-nature of the peak can result from varying amplitude or frequency of the variability change with time. After obtaining the frequency of these peaks, further interpretation regarding their origin can be made. An example is interpreting the kHz QPOs observed in a Neutron Star LMXBs in terms of the Keplerian frequency at the last stable circular orbit (a characteristic frequency of the system).

The Power Density Spectrum (PDS) can be obtained in a range of energy. Comparing different PDS in various energy bands provides information regarding the origin of variability. Since photons at different energies are known to be produced from other regions, one can infer which energy band has the most variability.

The method of obtaining a Power Spectrum is not trivial with real observations; one has to deal with discrete time data and not continuous data for which a Power

Spectrum is defined. The light curve extends from time $0 \to T$ consisting of N discrete measurements x_k taken at equally spaced time intervals $t_k = T/N$. A Fast Fourier Transform is used to calculate its Fourier Transform, which is an algorithm to compute the Discrete Fourier Transform (DFT) of a time series in much fewer computational steps. The DFT is defined as:

$$a_j = \sum_{k=0}^{N-1} x_k e^{-2\pi i jk/N} \quad (j = -N/2, \ldots, N/2 - 1)$$

where the frequencies are given by j/T, the time step is $\delta t = T/N$ and frequency step is $\delta v = 1/T$. This discreteness leads to a minimum and maximum cutoff to the frequency we can sample in the time series data. The minimum frequency is given by $\nu_{min} = 1/T$, whereas the maximum frequency is given by

$$\nu_{max} = \frac{1}{2\Delta t} = \frac{N}{2T}$$

This maximum frequency is called *Nyquist* frequency. Two things can be interpreted regarding the quality of our data. A long exposure time, i.e., the duration of the observation T, increases the minimum frequency one can sample in the Fourier Transform and not the sampling time of the signal. The Nyquist frequency increases with the signal's sampling (N), i.e., if more samples were taken for the same duration T, a higher frequency can be exposed in the Fourier Transform.

The Power Density Spectrum of a light curve can be modelled using multiple Lorentzian functions. An example fit is shown in Figure 2.2.
A Lorentzian L_i is defined with a characteristic centroid frequency ν_i. The total Power can be written as the sum of all the Lorentzian functions:

$$P(\nu) = \sum_{i=0}^{N-1} L_i(\nu)$$
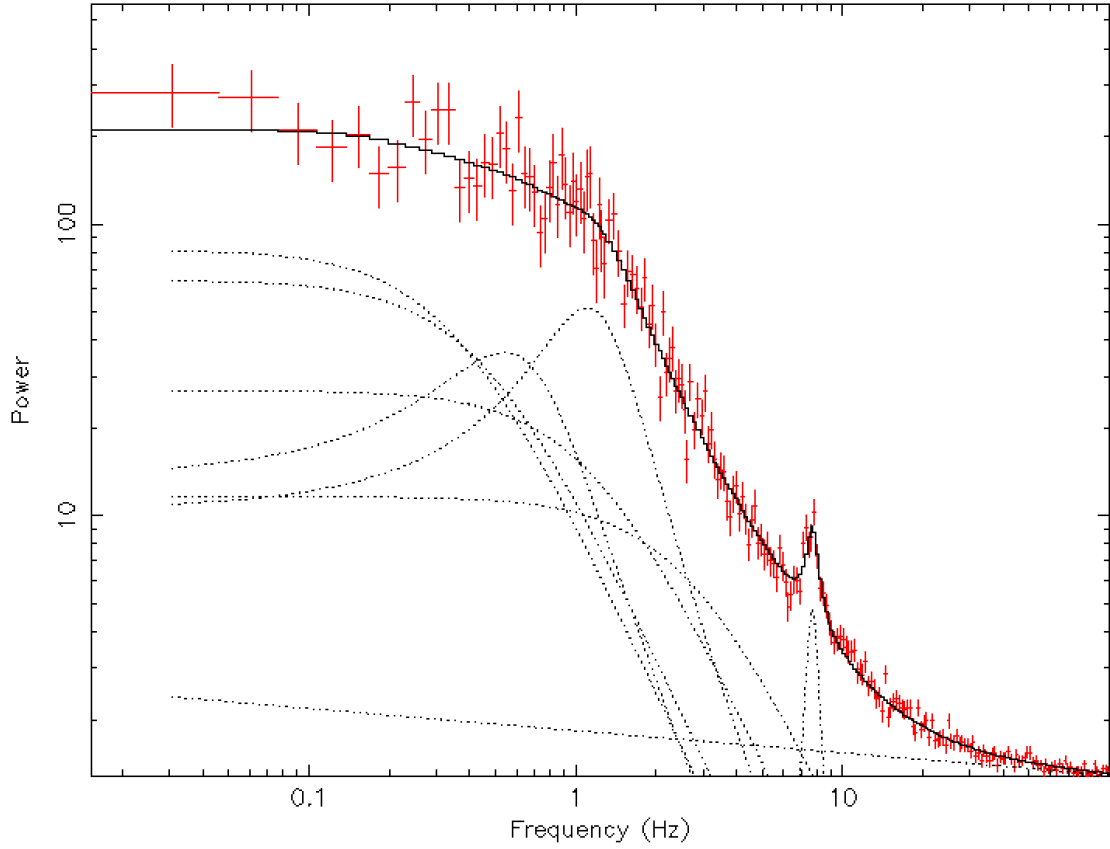
Figure 2.2: Example fit of a Power Density Spectrum using multiple Lorentzian function. A power law component was used to model the noise in the high frequency part of the spectrum.

where the formula for one single Lorentzian is:

$$L_i(\nu) = \frac{L_{i,0}^2}{\pi/2 + \tan^{-1}(\nu_i/\Delta_i)} \frac{\Delta_i}{\Delta_i^2 + (\nu - \nu_i)^2},$$

Here, v_i is the centroid frequency of the of Lorentzian component, Δ_i is the full width at half maximum (FWHM), and $L_{i,0}^2$ is a constant equal to the integral, over all frequencies, of that Lorentzian component. It has units of Power since we have obtained it after integrating over all frequencies for the Power Density Spectrum ($P(\nu)$vsν). Through Parseval's theorem, we can normalise the PDS such that

$$P(\nu) = \sum_{\nu_i} L_{i,0}^2$$

is equal to the square of the fractional root mean square (fractional rms) of the observed time series (Belloni and Hasinger, 1990). The fractional rms gives a measure of variability at a particular frequency defined by the Lorentzian component with respect to the mean variability in the light curve. This also allows us to compare the powers of different variability components as they are all normalised with respect to the mean variability. A quality factor $Q = \nu_0/\text{FWHM}$ is also defined for the Lorentzian component to quantify the coherence of a certain aperiodic signal. If the signal was fully periodic, then for $\text{FWHM} \to 0$, $Q \to \infty$. However, for aperiodic signals such as QPOs, the Q factor is low for broad features, and the FWHM is not 0. The Q factor gives the sharpness of the peak, and the more the Q factor, the sharper the peak, and for broad features, the Q factor is very low.

2.2.2 Phase Lags from Cross Spectrum

An effective approach to exploring the geometry of these systems' accretion flow is through the energy and frequency-dependent phase lags of the variability (Lewin et al., 1988). A cross-spectrum is used to obtain the phase lag value. Let the Fourier transform for two signals $f(t)$ and $g(t)$ be $F(\nu)$ and $G(\nu)$, respectively. The Cross spectrum between the two signals can be explained as:

$$CS(\nu_i) = F(\nu_i) \cdot C^*(\nu_i)$$

This cross-spectrum is a complex quantity, and at each frequency, ν_i, the argument of the cross-spectrum gives the phase lag between signals at that particular frequency (Belloni and Bhattacharya, 2022). The phase lags can also be converted to time lags by dividing $\delta\phi_{v_i}$ with an angular frequency $2\pi\nu_i$. Now, suppose the two initial signals were light curves from some LMXB in two different energy bands: $x(t, E_1)$ and $x(t, E_2)$. A phase lag obtained between these two signals at the QPO frequency

will provide information regarding the delay in signals ($\delta\phi_{v_i}$) at different energies at the QPO. This can explain the different processes that go behind producing signals in different energies and can allow one to infer a lot regarding the accretion geometry of the system. We can also infer the phase lag dependence on QPO frequency and its energy dependence.

2.3 Hardness Ratio

Hardness ratio values are used classify the spectral states of the system. A Hardness Ratio is defined as the ratio between the flux of Hard Photons and Soft Photons. If three energy bands are defined: A = 3 - 6 keV, B = 6 - 15 keV, and C = 15 - 60 keV and for each energy band the light curves are obtained. Then, the two hardness ratio counts are obtained as: HR1 = B/A and HR2 = C/A. When plotted against each other, the Color-Color diagram is obtained and when plotted against the total intensity, a Hardness Intensity diagram is obtained. Depending on the position of the observation on this Hardness Intensity Diagram, its spectral properties can be defined. This is discussed in detail in the next chapter.

Chapter 3

Literature Review

This section reviews work done on black hole X-ray binaries, particularly on GRS 1915+105. We will begin by discussing spectral and temporal variability canonical to BHXRB sources. Next, we will describe the recent work on the phase lag properties of type-C QPOs in GRS 1915+105.

3.1   GRS 1915+105

GRS 1915+105 was discovered on August 15, 2002, with the WATCH instrument on board GRANAT. This X-ray binary system in our Galaxy contains an accreting black hole of mass $12.4^{+2}_{1.8}M_{\odot}$ (Reid et al., 2014). This is a peculiar source as it never showed a complete Q-shape cycle in the Hardness Intensity Diagram. After its discovery, it was in the outburst phase for all these years before disappearing into a quiescent phase in 2021. GRS 1915+105 was also the first stellar-mass black hole in our Galaxy, displaying a superluminal radio jet (Méndez et al., 2022). This relativistic jet was similar to those observed in AGNs with a supermassive black hole. Much of the observational analysis on GRS 1915+105 was made possible because of observations from the Rossi X-ray Timing Explorer (RXTE) mission.

The properties discussed in the following sections were mainly studied using the RXTE observations.

3.2   Spectral States

A black hole X-ray binary is known to cycle through different spectral states where its luminosity changes orders of magnitude. This was suggested in the initial work on RXTE/PCA observations by Markwardt et al. (1999), who identified three different spectral states based on timing and spectral properties. Later work by Belloni et al. (2000), where they classified light curves into different variability classes and analysed the X-ray color color diagrams in detail, concluded that the flux and spectral variability of GRS 1915+105 and, in general, for BHXRBs can be classified into three states. The three spectral states were classified as:

1. **State A:** This state was classified as a soft state with significantly less time variability. The QPOs observed during this state were classified as type-A QPOs. Type-A QPOs have weak (very low fractional rms %) and broad peaks. These QPOs are not frequently observed. Photons from the accretion disk dominate the spectrum in this state.

2. **State B:** This state was also classified as a Soft or a Soft Intermediate state. Type-B QPOs have a relatively high amplitude and narrower peak than type-A QPOs. During this Soft Intermediate state, discrete jet ejections evidenced by transient radio flares have been shown (Fender and Belloni, 2004).

3. **State C:** The system changes its luminosity, going from a low hard state with significantly less luminosity to a high hard state with high luminosity, during this state while maintaining a relatively high hardness ratio. This state is known to show high variability in the X-ray emission. Type-C QPOs

are sharp (high Q factor), and strong (high fractional rms) features over the broadband noise. A number of harmonics are also observed along with the fundamentals. These are the most common types of QPOs observed due to their distinctive nature. This thesis focuses on the type-C QPOs detected in the source GRS 1915+105.
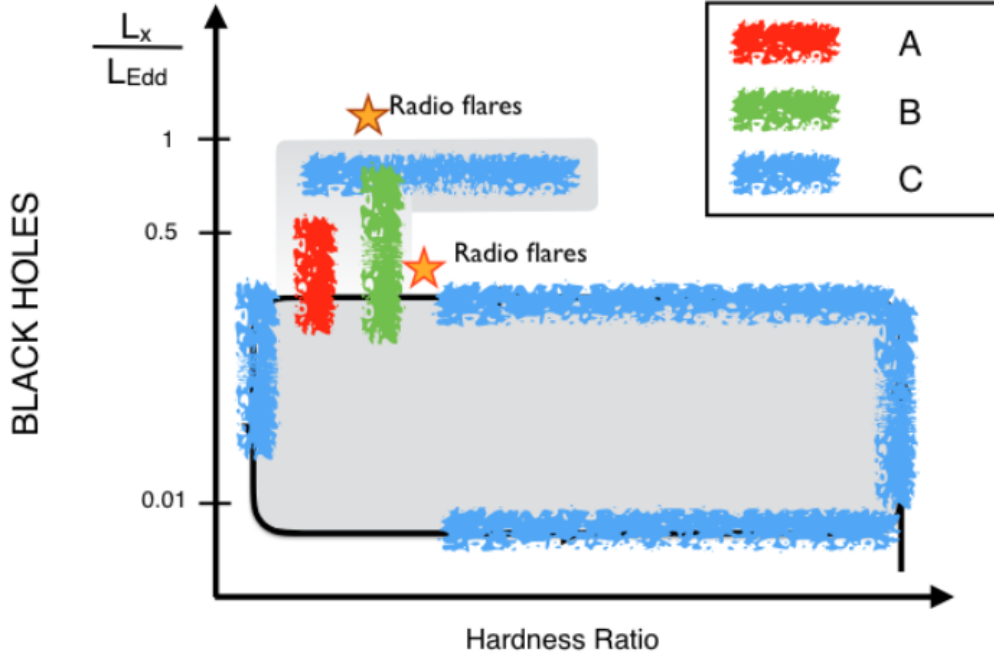
Figure 3.1: Types of QPOs observed in different parts of the Hardness Intensity Diagram. Credit: Muñoz-Darias et al. (2014)

Since accretion is the primary source of energy in the system, this change in luminosity and transitions into different spectral states was attributed to a change in the mass accretion rate (Miyamoto et al., 1992). The spectrum of the X-ray binary also becomes more soft/hard as it transitions between different spectral states. This spectrum also tells us information regarding the accretion geometry of the system. Thus, a study of how the source transitions between different spectral states can reveal changes in the system's accretion geometry and accretion flow. This change in the accretion geometry of the system can also explain the changes in the time

variability between different spectral states and the origin of the various types of QPO
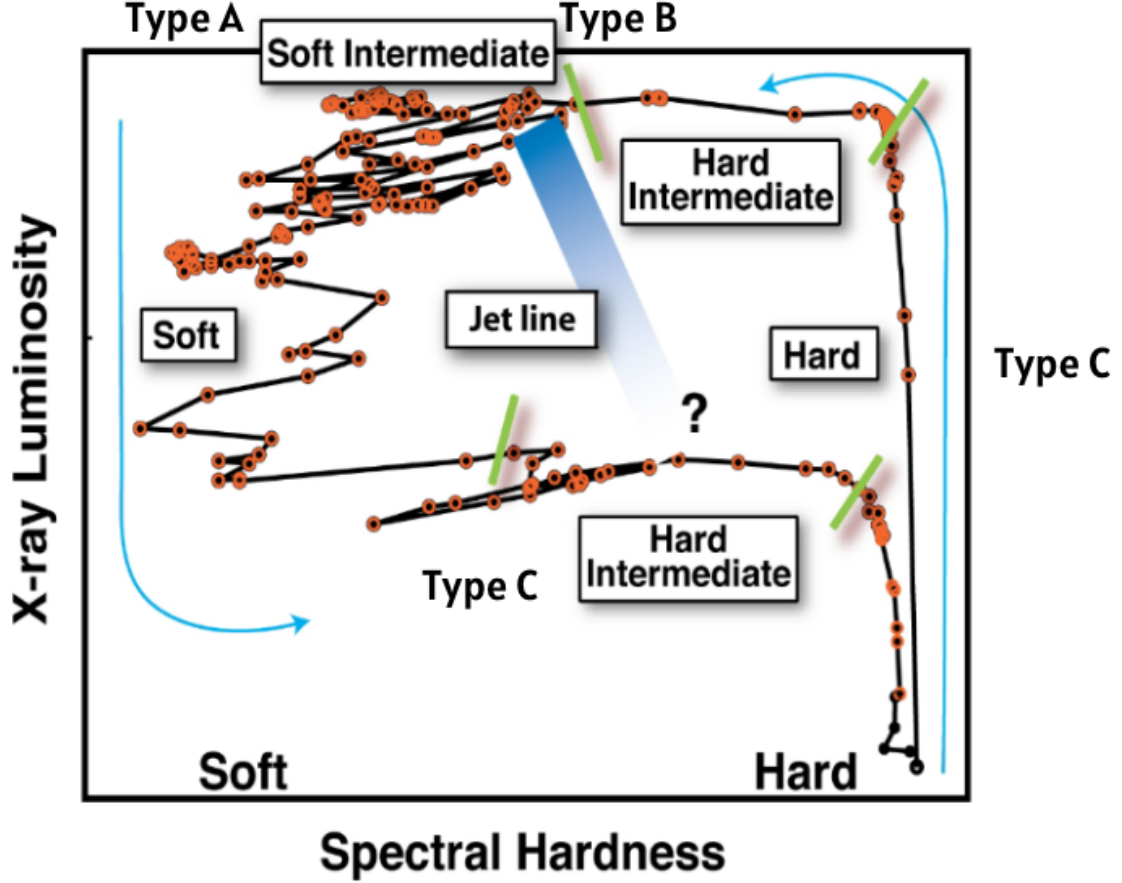
Figure 3.2: A Q-shape cycle in the Hardness Intensity Diagram (HID) for a BH XRB source GX 339-4. The blue arrow gives the direction of transition during the outburst phase. Credit: Karpouzas (2021)

A typical transition between these states resembles a Q-shape cycle, as shown in Figure 3.2. An outburst during which the source is observed begins as the source transitions from the Low Hard State to a Hard state, where its luminosity increases. In the Low Hard state, the luminosity is very low, but the source has a high Hardness ratio. After the luminosity increases and the source is in the Hard State, the source then transitions into the Soft state through two intermediate states: Hard Intermediate and Soft Intermediate. During these two intermediate states, the source luminosity remains more or less constant, but the HR decreases significantly. The

18

corona is believed to become less dominant and the disk more predominant as the source transitions into the soft state. Very low fractional variability is also observed as the source transitions to a soft state. The luminosity decreases while HR remains in the soft state. The loop is closed as the HR increases at low luminosity so that the source can return to the low hard state and quiescence period.

It is to be noted that not all BH LMXRB sources show exact transitions between different spectral states. However, this Q-cycle in the Hardness Intensity Diagram allows us to describe the general properties of a source observed during different spectral states and transitions.

3.3   Variability Classes in GRS 1915+105

A model-independent analysis of different variability classes in GRS 1915+105 was done by Belloni et al. (2000) using RXTE data. Based on the variability observed in the light curves and the color color diagrams, a total of 12 variability classes were classified. All variability classes were attributed to one of the spectral states described above.

The most observed variability class in their observations was χ. This variability class is associated with state C only and shows that the state remained in the hard state only. The QPO observed were in the range 1 Hz - 10 Hz further verifying that such a variability class is associated with the spectral state C only.
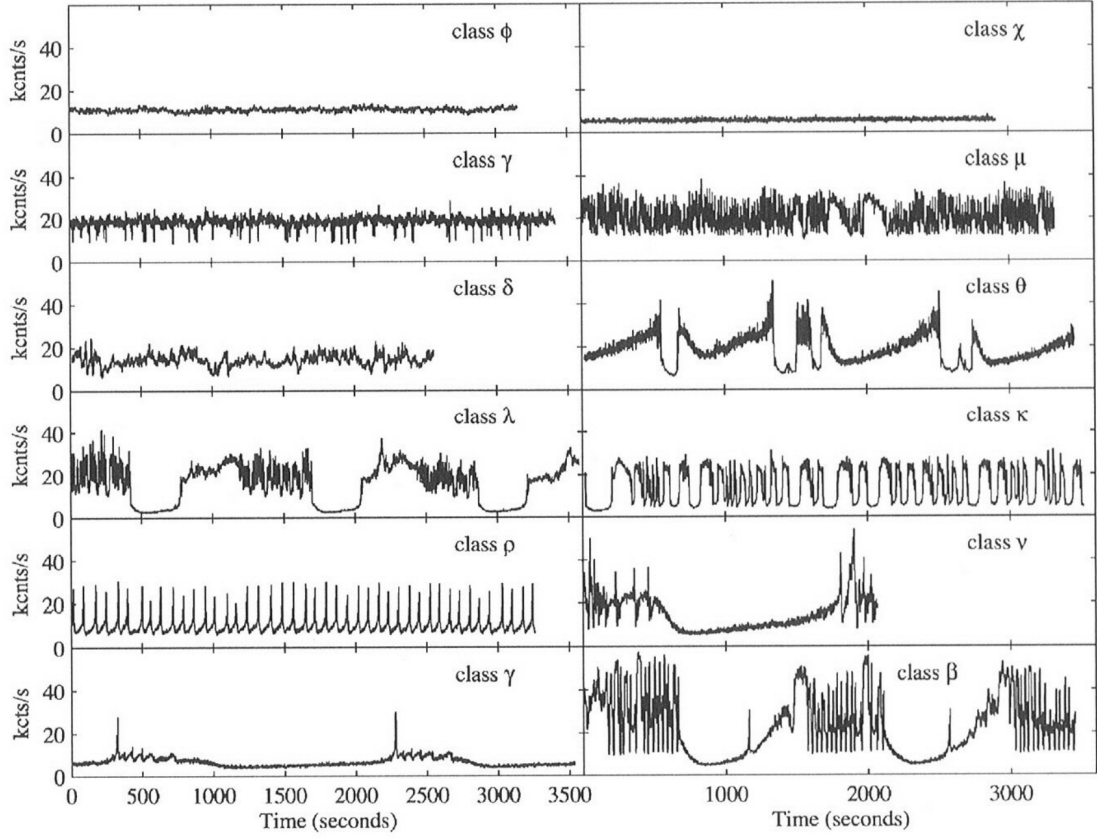
Figure 3.3: Sample light curves with 1-s binning from RXTE mission and their CCD for all 12 classes as defined in Belloni et al.

3.4   Variability Classes in GRS 1915+105 - AstroSat data

The timing analysis of selected intervals for most of the observations on GRS 1915+105 was done by Athulya et al. (2021). They classified 31 observations into different variability classes based on the classification done by Belloni et al. (2000). Out of the 31 observations, 13 observations were found to be in χ class, which is associated with state C. Other classes observed were HB ($\rho^{'}$), $\rho, \delta, \kappa \& \omega$.

20

3.5 Phase Lag analysis of GRS 1915+105 using RXTE data

A systematic analysis of the phase lags associated with the type-C QPOs in GRS 1915+105 using the RXTE data was done by Zhang et al. (2020). Their sample consisted of 620 RXTE observations with type-C QPOs ranging from ∼0.4 Hz to ∼6.3 Hz. The work presented in this thesis is in line with the analysis done by Zhang et al. (2020) but for all AstroSat observations. Their results confirmed hard lag associated with QPO frequencies below a break frequency of ∼ 2 Hz. Above ∼ 2 Hz, soft lags were observed. Strong QPO frequency dependence was shown for the phase lag slope.
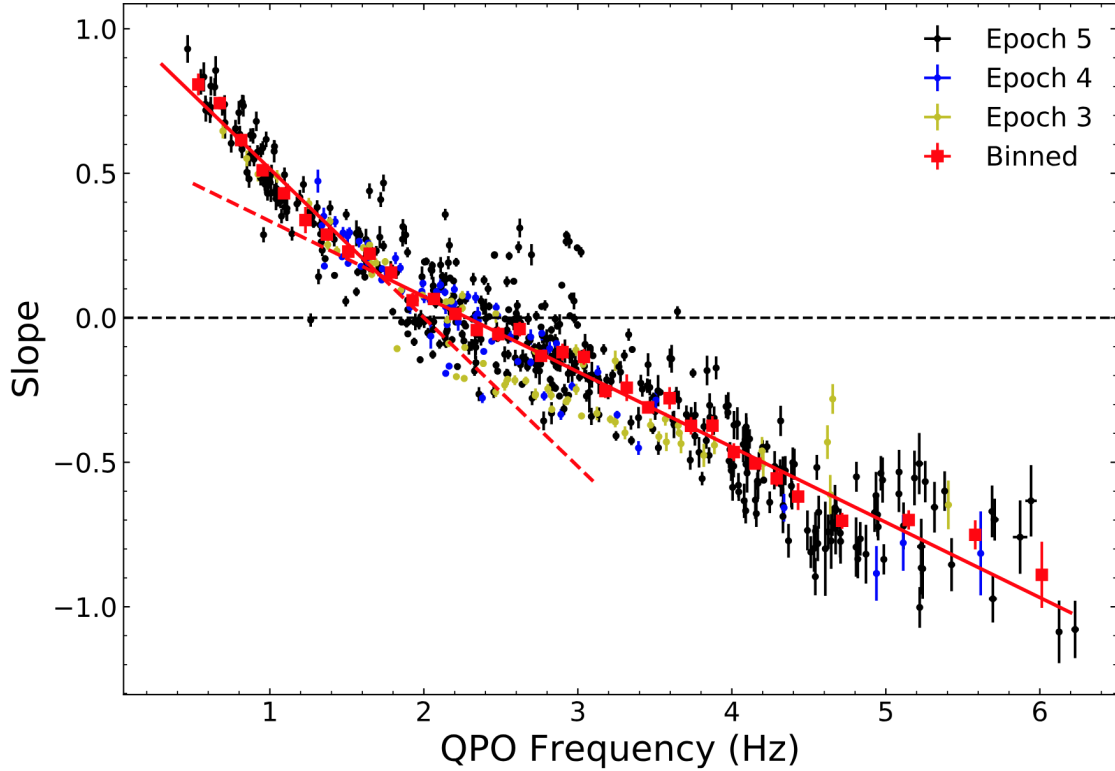
Figure 3.4: Results from Zhang et al. (2020): Slope of the lag-energy spectra evolution with QPO frequency, fitted with a broken line. Transition from soft lag to hard lag as the QPO frequency go below ∼ 2 Hz.

In addition, the slope was found to be different for QPOs below and above 2 Hz.

Figure 3.4 shows the slope of the QPO lag-energy spectra for the fundamental of type-C QPOs in GRS 1915+105. The solid line shows the best fitted broken line, for which the slope values are different. A similar trend was also observed for average phase lags (phase lag between 2-5.7 keV and 5.7-15 keV).

They also showed the dependence of fractional rms on QPO, which also showed different slope below and above ~ 2 Hz QPO frequency.
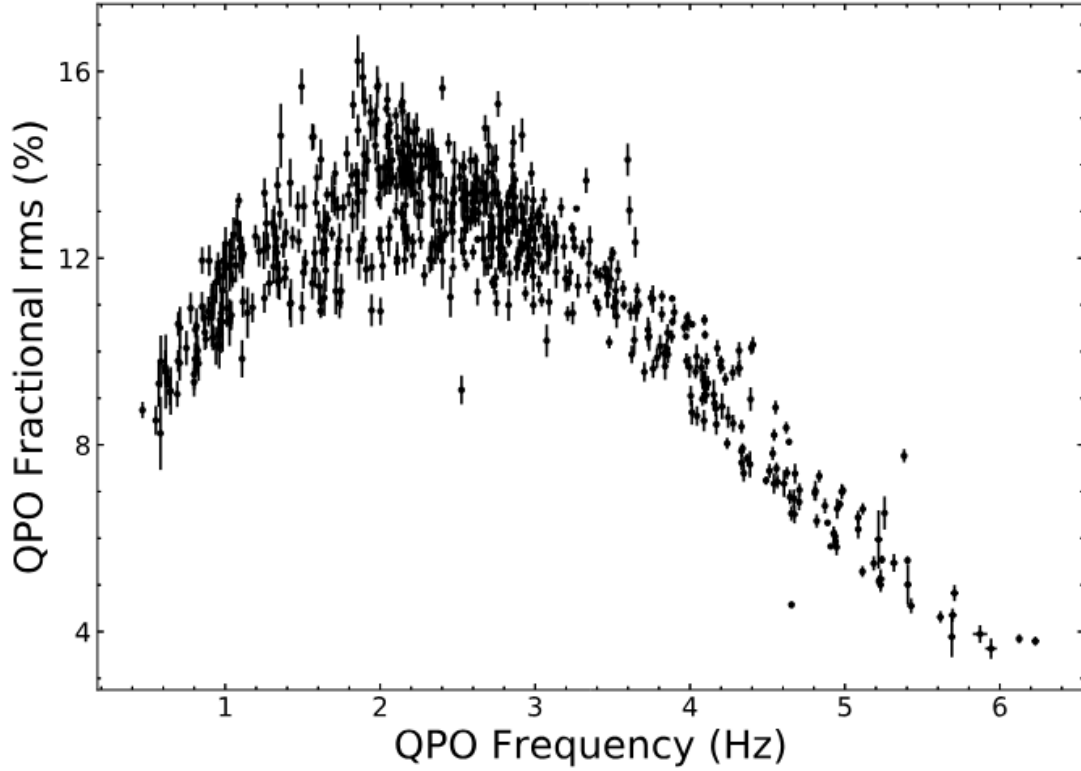
Figure 3.5: Results from Zhang et al. (2020): Fractional RMS of the QPO in full energy band of PCA against the QPO frequency of the fundamental. A similar break in the variability is observed below and above ~ 2 Hz.

3.6 Phase Lag analysis of GRS 1915+105 using AstroSat data

Recently, Belloni et al. (2023) performed an analysis on the phase lag and fractional rms properties of fundamental type-C QPO for an AstroSat observation. The light curve of this observation showed a U-shaped evolution in 10 hours. Such a U shape evolution is generally associated with periods of less than an hour or over days and months. As continuous data was available for a longer duration during this 10-hour period, a clear evolution of the type-C QPO with a high signal-to-noise ratio was possible. The QPO varied from a minimum of 2.55 Hz to a maximum of 6.61 Hz.
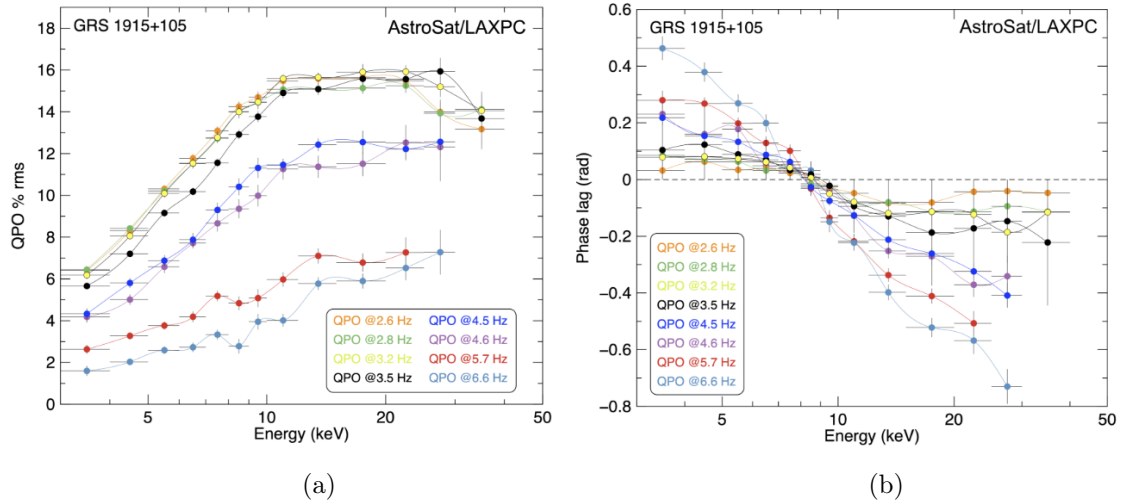
Figure 3.6: (a) Fractional RMS of the fundamental type-C QPOs as a function of energy. (b) Phase Lags (in radians) of the type-C QPOs as a function of energy. Both results show the same evolution (at a period of less than 10 hours) with energy and frequency as observed for a longer duration.

The phase lags vs energy, and the fractional rms vs energy graph showed the same evolution with energy and frequency of the fundamental QPO as was observed by Zhang et al. (2020). Using a variable Comptonization model developed by Bellavita et al. (2022), the energy spectrum, phase lag-energy spectrum and the fractional rms-energy spectrum were fitted simultaneously. More regarding the variable Comptonization model is discussed in the discussion section.

23

Chapter 4

Observations and Data Analysis

In this chapter, we will describe the AstroSat observations used for the analysis in this thesis. We will present the procedure followed to obtain the Power Density Spectrum and Phase Lags as a function of energy.

Observations

GRS 1915+105 was observed numerous times using the AstroSat/LAXPC instrument. The data used for this study is from 42 different observations (referred to by their Observational ID and called an epoch) from March 2016 to October 2020. These are level2 event files, which were obtained by processing the level1 files using the AstroSat LAXPC software. Each observation has data for multiple orbits, where one orbit duration usually lasts for about 90 minutes (each orbit data will be called an interval). The start and stop time information for each interval is provided in a Good Time Intervals file called a GTI file. Table A.2 in the Appendix shows all the observation IDs and the total number of intervals present in each observation. Further temporal and spectral analysis after obtaining the level 2 events file can be done either using the same LAXPC software or the GHATS analysis package. In

this project, most of the analysis was done using the GHATS package. The analysis involved producing the following files: light curve, background light curve, spectrum, background spectrum, power density spectrum (PDS) and Fast Fourier Transform (FFT). These files can be created for any/all LAXPC detector (1,2,3 or 123), layer (1,2,3,4,5 or 12345) and different energy levels (such as for a full band 3.0-80.0 keV or a soft band 3.0-4.0 keV).

4.1 Light Curve

A light curve is produced to observe the variability in brightness of the object over time. The classification of the light curves in terms of the variability classes has already been for most of the epochs by Athulya et al. (2021). Thus, the variability classes were all the epochs were taken from their results. For each interval, the average intensity was obtained by averaging out the light curve values.

4.2 Power Density Spectrum

Since eventually we wanted to obtain the phase lag behaviour for all individual intervals (interval is defined as the continuous data present in one good time interval), the power density spectrum was obtained for each interval data. The following procedure was followed for obtaining the Power Density Spectrum (in principle, all of this was done using a single command in GHATS):

1. A light curve with 1 ms ($100*10\mu$s) time binning for each interval was extracted and was divided into segments of 32.768 seconds. The values were chosen so as to keep the Nyquist frequency at 500 Hz and a sufficient total number of segments for further averaging the data. Total number of segments will be length of continuous data/32.768 seconds.

2. For each segment of 32.768 seconds, a Power Spectrum was obtained.

3. The Power Spectrum for all segments in an interval were then averaged out. This gave us one average power density spectrum per interval.

4. This procedure was applied to data for the full energy band as well as all 14 non-overlapping energy bands defined in Table **??**. Data from all the LAXPC units (1,2 and 3) and from all the layers (1,2,3,4 and 5) were considered.

5. The PDS obtained for all intervals were kept Leahy normalised.

The *ghats* command to obtain the Power Density Spectrum for an interval is as follows:

```
gh_laxpc_misra,'level2.event.fits','POWER',[3.0,50.0],123,12345,100,
32768,'result_file_name.pds',gti='gti_file_for_interval',ghx=ghx
```

Band	E_{low}	E_{high}
T	3	50
1	3	4
2	4	5
3	5	6
4	6	7
5	7	8
6	8	9
7	9	10
8	10	12
9	12	15
10	15	20
11	20	25
12	25	30
13	30	40
14	40	50

Figure 4.1: Energy boundaries (in keV) for the full energy band (reference band) and the other fourteen energy bands.

The Power Density Spectrum obtained for the entire energy band was then fitted using multiple Lorentzian functions. A constant component was used to model the Poissonian noise in the high-frequency region of the PDS. The number of Lorentzian used was dependent on the number of QPOs and harmonic features observed.

From the fitted model, the frequency of the fundamental QPO and its FWHM was noted. Table A.2,A.4 shows the QPO frequency and FWHM values for all epochs where a QPO was observed.

4.3 Phase Lags

The following procedure was followed to obtain Phase Lag spectrum for each interval data:

1. Fast Fourier Transform (FFT) files were obtained for all intervals in all 14 non-overlapping energy bands as well as the full energy band, which was used as the reference band.

2. A cross spectra was obtained for each FFT file with the reference band FFT file.

3. From the cross-spectra, the phase lags were computed at the QPO frequency by averaging the real and imaginary parts over a frequency band centred on the centroid frequency of the QPO and one FWHM wide. The values used for the centroid frequency of the QPO and FWHM were taken from the fitted values of the full energy band Power Density Spectrum. Although these values should be used from the individual energy bands for which phase lags need to be obtained, the QPO frequency was not found to vary much with energy. Moreover, the resulting phase lag values were similar when found at a QPO frequency from a PDS in a particular energy band and at the QPO frequency from a PDS in the full energy band (for the same interval).

4. Since the reference band chosen is the full energy band 3-50 keV, it also includes photons from all other bands. Thus, there is a zero-lag correlation for all cross-spectra. To account for this correction, we first obtained the cross-spectrum at

some high QPO frequency (say 300 Hz) and for very wide FWHM (say 400 Hz). The average value of the real part of the cross-spectrum was then subtracted (by giving it as a Poisson noise) from the output value before computing the lag.

The phase lag values at different energies for all intervals were obtained. This was called the Phase Lag Spectrum. Results from this analysis is shown in the next section.

Chapter 5

Results

In this chapter, we will present the results obtained from the analysis done on the AstroSat observations of GRS 1915+105. The results include the QPOs observed and phase lag vs energy spectrum at different QPO frequencies. In the appendix, a table is attached that contains the data of all the QPO frequencies, FWHM, and Q-factor values.

5.1 Observed QPOs

The centroid frequency of the fundamental, its FWHM and the Q-factor for the QPOs observed in all intervals are present in Table A.2 in the Appendix.

For our analysis, we selected observations where a significant QPO ($Q \gtrsim 2$) were observed. Out of the total 42 observations, 90 Low Frequency Q.P.O.s were observed. Figure 5.1 shows the distribution of the observed QPOs. The minimum QPO frequency observed was 0.17 Hz with a Q factor of 3.13, while the maximum QPO frequency observed in the Low-Frequency QPOs was 7.92 Hz with a Q factor of 3.98.
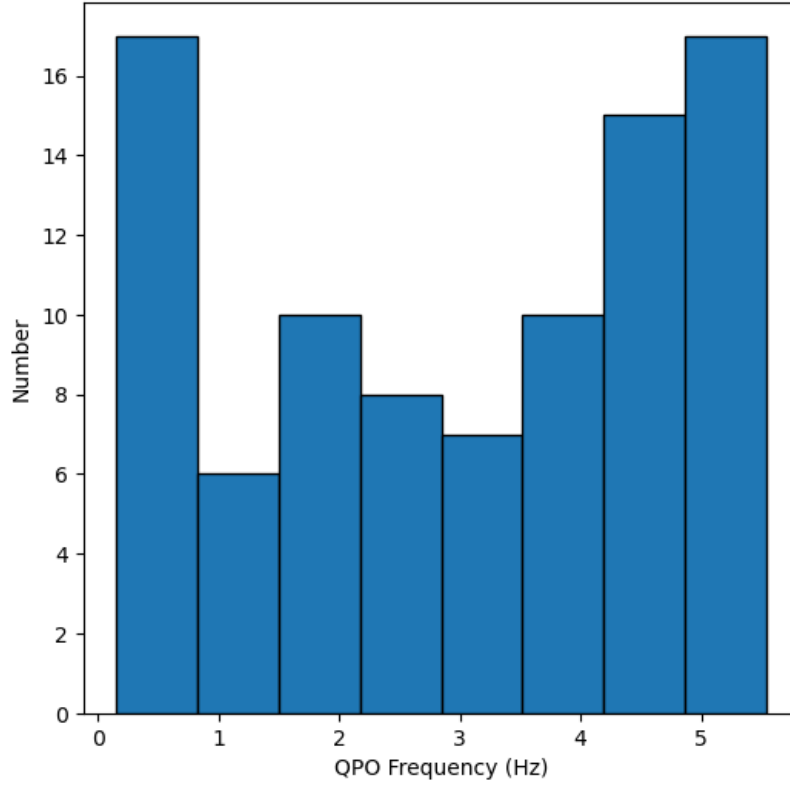
Figure 5.1: A distribution of all QPO frequencies observed for GRS 1915+105.

5.2 Phase Lags

The main result of this thesis is regarding the phase lag properties observed in GRS 1915+105. Since the phase lag properties were observed to change with the QPO frequencies, the interpretation of the results was made in two categories based on the phase lag properties. First, we will show results for observations with QPO centroid frequency between 2-7.92 Hz. Next, we will look at observations with QPO frequencies $\lesssim$ 2Hz.

5.2.1   Phase Lags between 2 Hz - 7.92 Hz

A total of 67 intervals showed QPO frequencies between 2 Hz - 7.92 Hz. Figure 5.2 shows a representative example of the Power Density Spectrum, Phase Lag spectrum between 3-4 keV energy band and 10-12 keV energy band with respect to the reference band 3-50 keV. It also shows the phase lag-energy spectrum, i.e., phase lags as a function of energy for the energy intervals described in the methods section. The upper limit to the phase lag-energy spectrum was decided based on whether a significant QPO was observed in the energy band. Usually, for higher energy bands, the QPO detection was not significant due to the low signal-to-noise ratio.
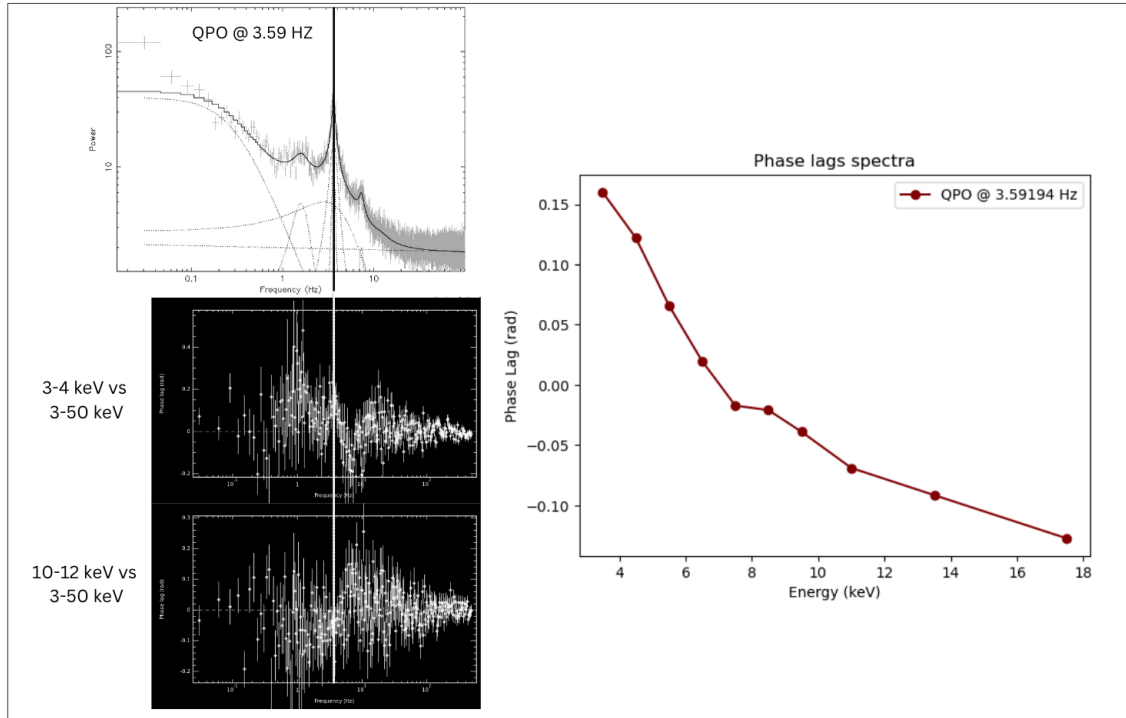
Figure 5.2: (a) (Top Left) Full energy band Power Spectrum with a QPO peak at 3.59 Hz. (b) (Middle Left) Phase Lag spectrum between the 3 - 4 keV energy band and the full energy band. The white line passing at QPO peak shows a positive lag value (c) (Bottom Left) Phase Lag spectrum between the 15 - 20 keV energy band and the full energy band. The white line passing at QPO peak shows a negative lag value. (d) (Bottom Right) Full Phase Lag Spectrum at different energies for the QPO peak observed at 3.59 Hz

Figure 5.3 shows the phase lag spectrum for QPOs at different frequencies. The

phase lags between 2 Hz and 7.92 Hz all show a soft lag (negative slope). This means that the soft photons are lagging behind the hard photons. Also, the negative slope of this phase lag vs energy graph consistently increases with the QPO frequency.

Figure 5.3: Phase Lags (in radians) of the QPOs between 2 Hz to about 7.92 Hz as a function of energy for the intervals described in the text. The reference energy band is the full band of 3-50 keV.

The following observations can be made from the above figures:

1. **QPO @ 2.4 Hz:** Figure (a) shows the phase lag vs energy graph for a QPO at about 2.4 Hz. The slope is not significantly different from a zero slope.

2. **QPO @ 3.3 Hz:** Figure (b) shows the phase lag vs energy for a QPO at about 3.3 Hz. The slope is negative, and a clear soft lag is observed. Values

from different observations but at the same QPO frequency show the same evolution, verifying that the Phase Lag Energy Spectrum is a clear function of QPO frequency.

3. **QPO @ 4.8 Hz:** Figure (c) shows the phase lag vs energy for a QPO at about 4.8 Hz. The slope has increased, and more soft lag is observed at higher QPO frequencies of 4.8 Hz than at lower QPO frequencies of 2.4 Hz or 3.3 Hz.

4. **QPO @ 7.92 Hz:** Figure (d) shows the phase lag vs energy for a QPO at about 7.92 Hz. An increased negative slope is observed compared to low frequencies, implying a strong, soft lag as the QPO frequency increases.

5.2.2 Phase Lags $\lesssim$ 2Hz

A total of 30 intervals showed QPO frequencies below 2 Hz. Figure 5.2 shows a representative example of the Power Density Spectrum, Phase Lag spectrum between the 3-4 keV energy band and 10-12 keV energy band with respect to the reference band 3-50 keV for a QPO frequency 0.52 Hz. It also shows the phase lag-energy spectrum, i.e., phase lags as a function of energy for the energy intervals described in the methods section and used for the above case.
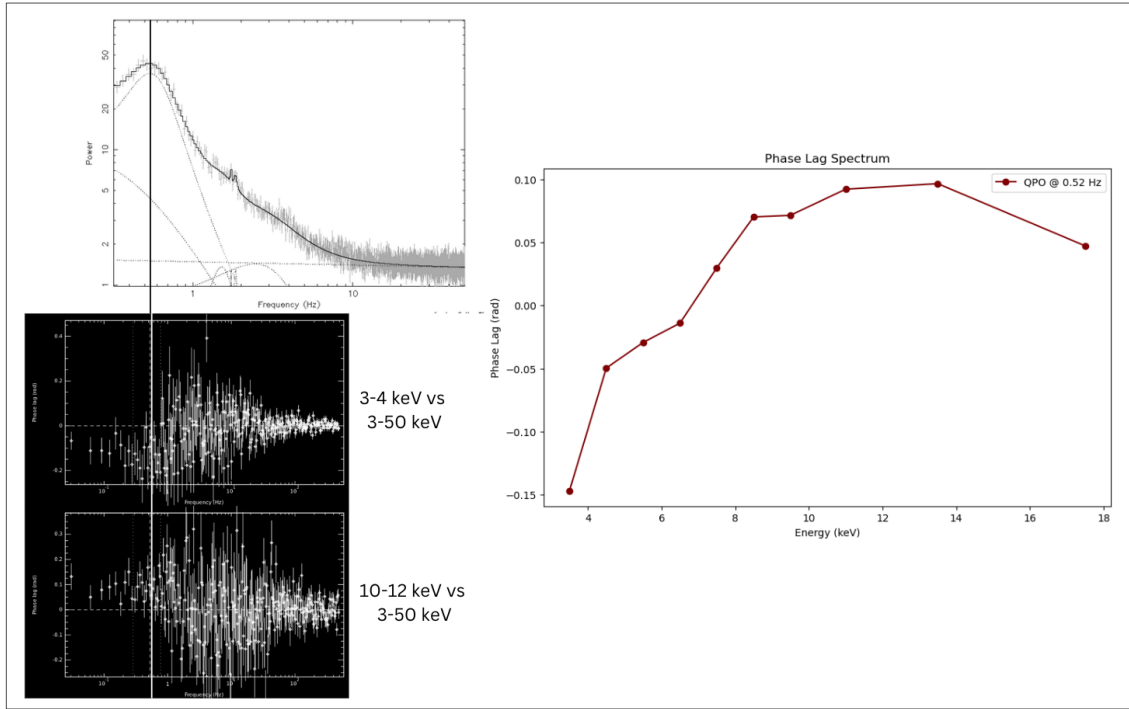
Figure 5.4: (a) (Top Left) Full energy band Power Spectrum with a QPO peak at 0.52 Hz. (b) (Middle Left) Phase Lag spectrum between the 3 - 4 keV energy band and the full energy band. The white line passing at QPO peak shows a negative lag value (c) (Bottom Left) Phase Lag spectrum between the 15 - 20 keV energy band and the full energy band. The white line passing at QPO peak shows a positive lag value. (d) (Right) Full Phase Lag Spectrum at different energies for the QPO peak observed at 0.52 Hz.

Figure 5.5 shows the phase lag spectrum for QPOs at different frequencies. The phase lags below 2 Hz all show a hard lag (positive slope or near zero slope). This means that the hard photons are lagging the soft photons. Also, the negative slope of this phase lag vs energy graph consistently increases with the QPO frequency, implying higher hard lag at low-frequency QPOs.
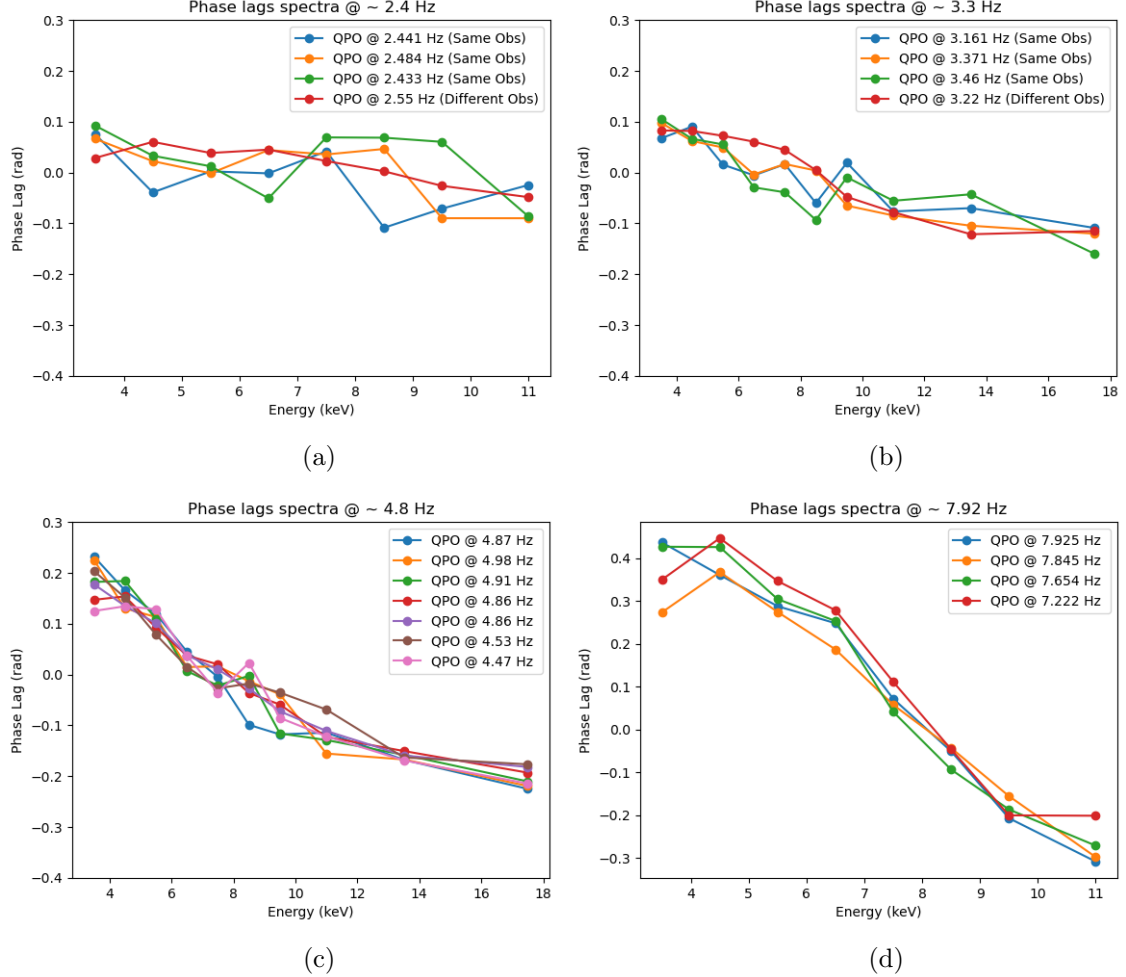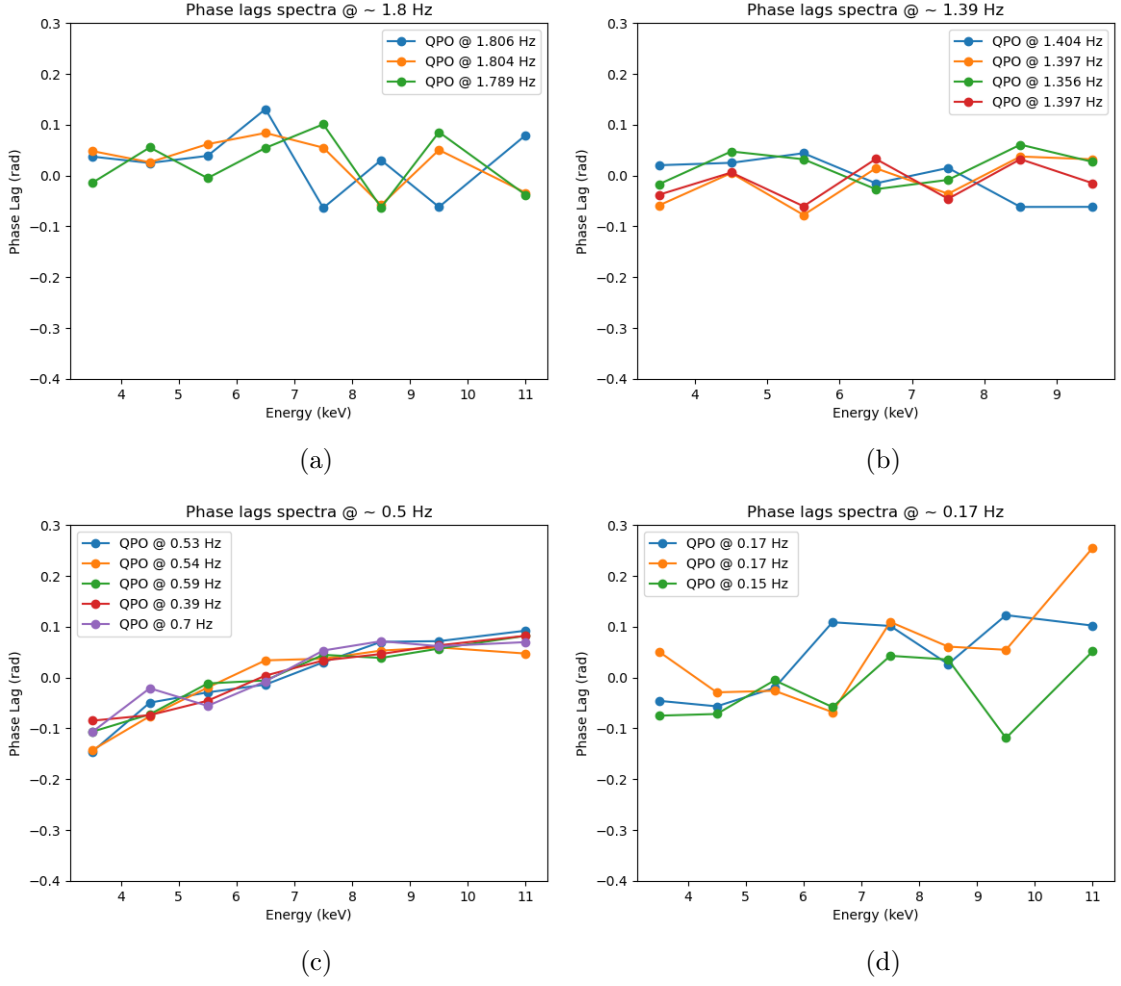
Figure 5.5: Phase Lags (in radians) of the QPOs less than 2 Hz as a function of energy for the energy intervals described in the text. The reference energy band is the full band of 3-50 keV.

The following observations can be made from the above figures:

1. **QPO @ 1.89 Hz:** Figure (a) shows the phase lag vs energy graph for a QPO at about 1.89 Hz. The slope is not significantly different from a zero slope. Around this frequency, Zhang et al. (2020) have shown that a transition from Soft Lag to Hard Lag happens as the QPO frequency decreases.

2. **QPO @ 1.39 Hz:** Figure (b) shows the phase lag vs energy for a QPO at about 1.39 Hz. Although the slope can not be significantly differentiated from a zero lag slope, the initial lag values at low energies are negative, while at higher energies, they are positive. This implies that the slope is positive and

there is a hard lag.

3. **QPO @ 0.52 Hz:** Figure (c) shows the phase lag vs energy for a QPO at about 0.52 Hz. The positive slope has increased, and clear hard lag is observed at a lower QPO frequency of 0.52 Hz compared to higher QPO frequencies of 1.8 Hz or 1.4 Hz. Since no QPOs were detected between the range 0.5 Hz and 1.4 Hz, a clear evolution in the hard lag can not be made as was done for Soft lags.

4. **QPO @ 0.17 Hz:** Figure (d) shows the phase lag vs energy for a QPO at about 0.17 Hz. Again, the initial lag values at low energies are negative, while at higher energies, they are positive, implying hard lag. Since the detection of QPOs at such a low frequency was not significant in different energy bands, the phase lag values do not show clear evolution with energy.

5.3 Phase Lag Slope vs QPO frequency

For all the phase lag vs energy spectrum, a straight line was fitted for the first eight energy intervals for which the phase lag values were available for the complete data set. Figure 5.6 shows a clear relationship between the slope of the spectrum and the QPO frequency. A transition from soft to hard lag is seen at about 2 Hz. However, no clear break in the slope was observed here, which was reported by Zhang et al. (2020) about this transition point. The reasons for this could be either related to the fact that fewer observations were available in the range of QPO less than 2 Hz or that we fitted the straight slope through the first eight energy intervals only. In any case, the transition from soft to hard lags still occurs approximately near 2 Hz, which can be seen in the figure below.
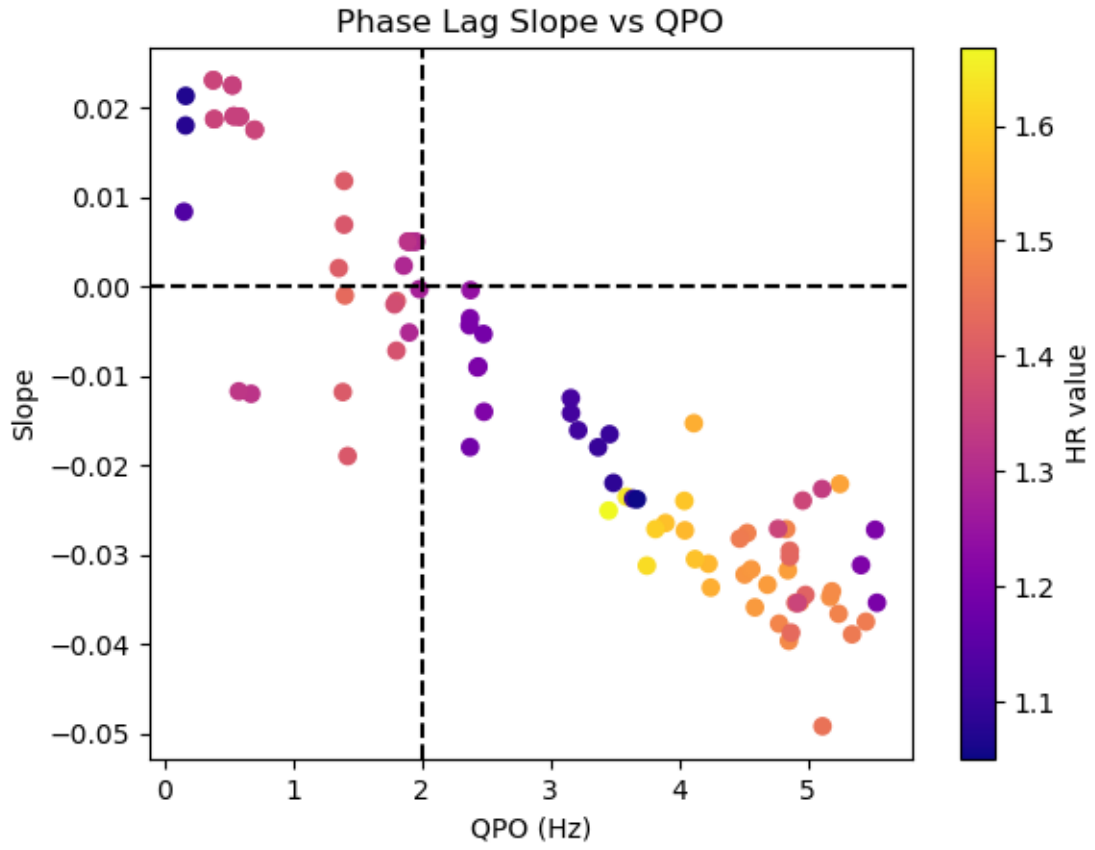
Figure 5.6: Slope for the Phase Lag vs Energy spectrum plotted against QPO frequency. A strong dependence on QPO frequency is observed for the Phase Lags.

Chapter 6

Discussion and Conclusion

In this chapter, we briefly discuss the interpretation of the observed results. This is a qualitative interpretation. We then discuss the scope in which the current project can be extended. This includes a quantitative description of corona variability using the variable Comptonization model and studying the coupling between phases of fundamental QPO and its harmonics using higher-order statistics.

6.1   Physical Interpretation of Results

We present the systematic analysis of phase lags associated with the type-C QPOs in GRS 1915+105, using observational data available from AstroSat. Our sample comprises of 90 intervals (continuous data segments) from 42 observations. The QPO frequency in the data ranges from 0.17 Hz to 7.92 Hz. Phase lag spectrum for all the intervals were obtained. The following conclusions were made:

1. The phase lag-energy spectrum slope was shown to be strongly dependent on the QPO frequency.

2. Around ~ 2 Hz, the phase lag spectrum slope changed from soft to hard lag.

No break in the phase lag slope was conclusively found below and above ~ 2 Hz as observed by Zhang et al. (2020).

Several models have been proposed to explain this phase lag behaviour. Initially, Nobili et al. (2000) suggested a two-component corona thermal Comptonization model. For QPOs > 2 Hz, the inner component was hot and optically thick which increased temperature of all photons to 15 keV but then the outer optically thin corona down scatter the hard photons, which result in soft lags. For QPOs < 2 Hz, the corona is optically thin, and the soft photons will only experience a delay due to Compton scattering; thus, the lags will be hard. Here, the change in the lag sign was attributed to changes in the optical depth of the corona and the inner radius of the disc.

Karpouzas (2021) built a Comptonization model that explained the soft lag as delayed heating of the soft photon source (accretion disk) by the previously up-scattered photons in the Corona. The heating of the soft photon source was termed the feedback effect. Different accretion geometries will have different feedback fractions. The changes in the accretion geometry here refer to the change in the corona size and the inner radius of the accretion disk.

The following explanation was built based on the results and explanation by Karpouzas (2021), García et al. (2022) and Belloni et al. (2023). Suppose the feedback fraction was assumed to be zero. In that case, the time delay due to the Comptonization process will delay the escaping of hard photons from the Corona due to more scatterings required to reach higher energies compared to soft photons escaping from the accretion disk. In this case, a hard lag should be observed. However, the results show that sometimes there is a Soft, Hard, and Zero lag depending on the QPO frequency.

Now, if the corona size is assumed to be large and it covers say half of the accretion

42

disk, then the feedback fraction will be high. This is because the up-scattered photons will have a high probability of hitting back to the disk. After all, half of the sky for the photons in the corona is covered by the accretion disk. Thus, if a large number of photons from the corona come back to the disk, there will be a high feedback fraction. The accretion disk will be heated through a feedback process, and the soft photons will emerge after the disk has reached temperature to emit a large amount of soft energy photons. It is to be noted that the initial temperature of the disk can be very low compared to the soft photons where the lag is measured.

To explain the soft lag (say at a high QPO of 6 Hz), there is a high feedback fraction and a larger corona covering most of the accretion disk. Time delay due to high feedback fraction heating will cause soft lag. As the QPO frequency decreases, the inner edge of the accretion disk moves outwards, and the corona also decreases. In this case, the magnitude of the lags will decrease, which was observed as the QPO frequency decreased from 6 Hz to $\sim$ 2 Hz. At the QPO frequency of 2 Hz, the feedback fraction is very low, and no part of the corona covers the accretion disk. Below 2 Hz, the disk goes further out, and thus, the time delay due to Comptonization from the corona for high energy photons dominates over the time delay due to feedback heating.

6.2   Scope for Future Work

Here, a qualitative discussion was provided based on previous results obtained by Karpouzas (2021), García et al. (2022) and Belloni et al. (2023). The future work involves using the model developed by Bellavita et al. (2022) to fit the energy spectrum, phase lag - energy spectrum, and the fractional rms - energy spectrum. This analysis will allow quantitative answers to the changes in accretion geometry of the system at different QPO frequencies as observed for GRS 1915+105 using the

AstroSat observations from 2015-2021.

Another possible work can be to study the phase coupling for the fundamental QPO and the harmonics present using higher order statistical techniques such as 'bi-coherence'. A bi-spectrum provides a correlation between phases of Fourier Components at three frequencies and provides information about non-linear interaction between waves. Recently Arur and Maccarone (2022) observed different bi-coherence patterns for the same type of Power Spectra. The different bi-coherence patterns also show different behaviour around the 2 Hz QPO frequency mark. They also studied the correlation of this bi-coherence behaviour at different QPOs with the radio properties shown by the source.

Simultaneous radio observations allow us to study the correlation between X-ray timing and spectral properties and the radio emission from the jets. Recently, Méndez et al. (2022) provided evidence that the energy that powers an accreting black-hole system can be directed either to the X-ray corona or the jet. They conclusively showed that the X-ray corona morphs into the jet. Thus, a multi-wavelength analysis in both X-rays and radio bands is the way to improve our understanding of the accretion geometry and physical mechanisms that power the jet in all accreting sources.

Bibliography

Agrawal, P. C., Yadav, J. S., Antia, H. M., Dedhia, D., Shah, P., Chauhan, J. V., Manchanda, R. K., Chitnis, V. R., Gujar, V. M., Katoch, T., Kurhade, V. N., Madhwani, P., Manojkumar, T. K., Nikam, V. A., Pandya, A. S., Parmar, J. V., Pawar, D. M., Roy, J., Paul, B., Pahari, M., Misra, R., Ravichandran, M. H., Anilkumar, K., Joseph, C. C., Navalgund, K. H., Pandiyan, R., Sarma, K. S., and Subbarao, K. (2017). Large area x-ray proportional counter (laxpc) instrument on astrosat and some preliminary results from its performance in the orbit. *Journal of Astrophysics and Astronomy*, 38(2).

Arur, K. and Maccarone, T. J. (2022). Using the bispectrum to probe radio x-ray correlations in grs 1915+105. *Monthly Notices of the Royal Astronomical Society*, 514(2):1720–1732.

Athulya, M. P., Radhika, D., Agrawal, V. K., Ravishankar, B. T., Naik, S., Mandal, S., and Nandi, A. (2021). Unravelling the foretime of grs 1915+105 using astrosat observations: Wide-band spectral and temporal characteristics. *Monthly Notices of the Royal Astronomical Society*, 510(2):3019–3038.

Bambi, C. and Sangangelo, A. (2022). *Handbook of X-ray and Gamma-ray Astrophysics*.

Bellavita, C., García, F., Méndez, M., and Karpouzas, K. (2022). vkompth: a variable comptonization model for low-frequency quasi-periodic oscillations in

black hole x-ray binaries. *Monthly Notices of the Royal Astronomical Society*, 515(2):2099–2109.

Belloni, T. and Hasinger, G. (1990). An atlas of aperiodic variability in HMXB. , 230:103–119.

Belloni, T., Klein-Wolt, M., Mendez, M., van der Klis, M., and van Paradijs, J. (2000). A model-independent analysis of the variability of grs 1915+105.

Belloni, T. M. and Bhattacharya, D. (2022). *Basics of Fourier Analysis for High-Energy Astronomy*, page 1–34. Springer Nature Singapore.

Belloni, T. M., Mendez, M., Garcia, F., and Bhattacharya, D. (2023). Fast-varying time lags in the quasi-periodic oscillation in grs 1915+105.

Fender, R. and Belloni, T. (2004). Grs 1915+105 and the disc-jet coupling in accreting black hole systems. *Annual Review of Astronomy and Astrophysics*, 42(1):317–364.

García, F., Karpouzas, K., Méndez, M., Zhang, L., Zhang, Y., Belloni, T., and Altamirano, D. (2022). The evolving properties of the corona of grs 1915+105: a spectral-timing perspective through variable-comptonization modelling. *Monthly Notices of the Royal Astronomical Society*, 513(3):4196–4207.

Karpouzas, K. (2021). *Modelling of Comptonisation in low-mass X-ray binaries in the presence of fast variability*. PhD thesis, University of Groningen.

Lewin, W. H. G., van Paradijs, J., and van der Klis, M. (1988). A review of quasi-periodic oscillations in low-mass X-ray binaries. , 46(3-4):273–377.

Markwardt, C. B., Swank, J. H., and Taam, R. E. (1999). Variable-frequency quasi-periodic oscillations from the galactic microquasar grs 1915+105. *The Astrophysical Journal*, 513(1):L37–L40.

Miyamoto, S., Kitamoto, S., Iga, S., Negoro, H., and Terada, K. (1992). Canonical Time Variations of X-Rays from Black Hole Candidates in the Low-Intensity State. , 391:L21.

Muñoz-Darias, T., Fender, R. P., Motta, S. E., and Belloni, T. M. (2014). Black hole-like hysteresis and accretion states in neutron star low-mass x-ray binaries. *Monthly Notices of the Royal Astronomical Society*, 443(4):3270–3283.

Méndez, M., Karpouzas, K., García, F., Zhang, L., Zhang, Y., Belloni, T. M., and Altamirano, D. (2022). Coupling between the accreting corona and the relativistic jet in the microquasar grs 1915+105. *Nature Astronomy*, 6(5):577–583.

Nobili, L., Turolla, R., Zampieri, L., and Belloni, T. (2000). A Comptonization Model for Phase-Lag Variability in GRS 1915+105. , 538(2):L137–L140.

Reid, M. J., McClintock, J. E., Steiner, J. F., Steeghs, D., Remillard, R. A., Dhawan, V., and Narayan, R. (2014). A parallax distance to the microquasar grs 1915+105 and a revised estimate of its black hole mass. *The Astrophysical Journal*, 796(1):2.

Zhang, L., Méndez, M., Altamirano, D., Qu, J., Chen, L., Karpouzas, K., Belloni, T. M., Bu, Q., Huang, Y., Ma, X., Tao, L., and Wang, Y. (2020). A systematic analysis of the phase lags associated with the type-c quasi-periodic oscillation in grs 1915+105. *Monthly Notices of the Royal Astronomical Society*, 494(1):1375–1386.

Appendix A

Results: Observed QPOs data

Interval	Fundamental QPO (v)	FWHM	Q-factor
Observation ID: T01_030T01_9000000358			
19	5.67	0.70	8.10
20	6.61	0.67	9.87
21	4.60	0.45	10.22
22	4.50	0.50	9.00
24	3.54	0.46	7.70
25	2.55	0.32	7.97
26	2.79	0.36	7.75
27	3.22	0.41	7.85
Observation ID: G06_033T01_9000000760			
1	7.92	1.99	3.98
2	7.84	1.34	5.85
3	7.65	0.79	9.71
4	7.22	0.61	11.88
Observation ID: G07_046T01_9000001124			
1	3.90	0.71	5.46
2	4.51	1.43	3.16
3	4.05	0.64	6.27
5	3.82	0.65	5.86
6	4.04	0.72	5.65
8	4.56	1.22	3.75
9	4.85	1.13	4.28
10	5.11	0.92	5.56

Table A.1: Details of model fitted parameters for 3 Observation IDs.

Interval	Fundamental QPO (v)	FWHM	Q-factor
Observation ID: G06_033T01_9000001116			
1	3.63	0.35	10.23
2	3.59	1.45	2.48
3	3.45	0.52	6.68
4	3.75	0.56	6.75
5	4.23	1.14	3.70
6	4.12	0.70	5.88
7	4.25	0.57	7.40
8	4.59	0.86	5.33
10	4.69	1.09	4.30
11	4.12	9.25	0.45
12	4.85	1.24	3.92
13	5.25	1.02	5.16
14	5.17	1.28	4.03
15	5.24	0.88	5.96
16	5.19	0.90	5.74
17	4.78	0.82	5.79
18	4.94	0.93	5.31
19	5.45	1.46	3.73
20	5.34	1.53	3.49
21	4.83	0.44	11.06
Observation ID: G07_046T01_9000001162			
1	4.87	0.64	7.62
2	4.98	0.75	6.68
3	4.91	0.69	7.12
4	4.86	0.65	7.47
5	4.86	0.70	6.96
6	4.53	0.87	5.19
7	4.47	0.33	13.60
Observation ID: G07_028T01_9000001166			
1	4.79	0.89	5.39
Observation ID: G07_028T01_9000001232			
1	4.96	0.88	5.66
2	4.77	0.61	7.87
3	4.92	0.65	7.54
4	5.11	0.62	8.18
Observation ID: G07_046T01_9000001236			
2	5.54	1.01	5.50
3	5.52	1.18	4.69
7	5.41	0.93	5.84

Table A.2: Details of model fitted parameters for 5 Observation IDs.

Interval	Fundamental QPO (v)	FWHM	Q-factor
Observation ID: G07_028T01_9000001272			
3	0.68	0.32	2.14
6	0.58	0.37	1.56
Observation ID: G07_046T01_9000001506			
1	69.01	0.12	569.39
2	68.91	0.10	690.17
1	0.53	0.49	1.09
2	0.54	0.46	1.18
3	0.59	0.31	1.90
4	0.39	0.50	0.78
5	0.70	0.12	5.73
7	0.38	0.67	0.57
Observation ID: G07_046T01_9000001506			
1	0.53	0.49	1.09
2	0.54	0.46	1.18
3	0.59	0.31	1.90
4	0.39	0.50	0.78
5	0.70	0.12	5.73
7	0.38	0.67	0.57
Observation ID: A04_180T01_9000001622			
1	3.35	1.65	2.03
Observation ID: A04_180T01_9000002000			
1	3.64	1.04	3.50
Observation ID: G08_028T01_9000002006			
	3.67	0.66	5.58
Observation ID: G08_028T01_9000002080			
2	2.38	0.30	7.95
3	2.44	0.37	6.52
4	2.48	0.32	7.73
5	2.43	0.34	7.10
6	2.48	0.36	6.81
7	2.38	0.26	8.98
8	2.38	0.62	3.83
9	2.37	0.33	7.19

Table A.3: Details of model fitted parameters for 7 Observation IDs/

Interval	Fundamental QPO (v)	FWHM	Q-factor
Observation ID: G08_028T01_9000002112			
1	3.16	0.44	7.26
2	3.16	0.39	8.13
3	3.22	0.38	8.48
4	3.37	0.42	7.97
5	3.49	0.47	7.46
6	3.46	0.43	8.04
Observation ID: G08_028T01_9000002220			
1	1.98	0.17	11.38
2	1.86	0.15	12.72
3	1.90	0.16	11.67
4	1.98	0.17	11.34
5	1.97	0.18	10.74
6	1.96	0.14	13.92
7	1.93	0.13	14.51
8	1.90	0.14	13.57
9	1.89	0.16	12.08
Observation ID: G08_028T01_9000002306			
1	1.40	0.15	9.08
2	1.40	0.11	13.05
3	1.36	0.18	7.38
4	1.39	0.12	11.83
5	1.40	0.13	11.10
6	1.42	0.16	8.76
Observation ID: G08$_0$28T01$_9$000002334			
2	1.81	0.20	8.83
3	1.80	0.18	10.20
7	1.79	0.12	14.75
1	0.41	0.01	45.86
Observation ID: T04$_0$29T01$_9$000004582			
1	0.17	0.08	2.12
2	0.17	0.05	3.13
5	0.15	0.13	1.18

Table A.4: Details of model fitted parameters for 3 Observation IDs.